Evidence of Spiro-OMeTAD De-doping by tert-Butylpyridine Additive in Hole-Transporting Layers for Perovskite Solar Cells

Evidences of de-doped Spiro-OMeTAD employing tert-butyl pyridine as additive in hole-transporting layers for n-i-p perovskite photovoltaics

Francesco Lamberti[*1,2,4], *Teresa Gatti*[1], *Enrico Cescon*[1], *Roberto Sorrentino*[2], *Antonio Rizzo*[3], *Enzo Menna*[1], *Gaudenzio Meneghesso*[3], *Moreno Meneghetti*[1], *Annamaria Petrozza*[2], *Lorenzo Franco**[1]

[1] Department of Chemical Sciences, University of Padova, Via Marzolo 1, 35131 Padova, Italy

[2] Center for Nanoscience and Technology, Italian Institute of Technology, Via Pascoli 70/3, 20133 Milano, Italy

[3] Department of Information Engineering, University of Padova, Via Gradenigo 6/a, 35131 Padova, Italy

[4] Lead contact

* Correspondence: francesco.lamberti@unipd.it (F.L.); lorenzo.franco@unipd.it (L.F.)

Summary

Spiro-OMeTAD is the mostly employed molecular hole transporting material (HTM) in n-i-p perovskite solar cells (PSCs). Ease of processing from solution and good filmability on top of the perovskite photo-active layer are characteristics that make this HTM outstanding and incomparable for the role. However, both chemical doping with tert-butylpyridine (tBP) and lithium bis(trifluoromethylsulfonyl)-imide (LiTFSI), coupled to further oxidation steps, are required in order to achieve high hole mobility and conductivity. Previous investigations revealed that tBP is fundamental for addressing the best morphology in the hole-transporting layer during processing. We provide here for the first time a spectroscopic evidence of the detrimental impact on long-term conservation of Spiro-OMeTAD structural and electrical properties when tBP is used as additive. These aspects are crucial for the future design and understanding of new molecular HTMs for PSCs.

KEYWORDS SPIRO-OMeTAD; de-doping; degradation; halide perovskite; hole-transporting material, tert-butyl pyridine.

Introduction

Since the beginning of active research on perovskite solar cells (PSCs), the Spiro-OMeTAD molecule ([2,2′,7,7′-tetrakis(N,N-di-p-methoxyphenyl-amine)9,9′-spirobifluorene], from now on

SPIRO), has been the most employed hole transporting material (HTM) in such devices.[1] The main reason relies on the possibility of obtaining the highest figures of merit on as-prepared PSCs, due to SPIRO good wettability on top of the perovskite layer. This property is related to its inherent tridimensional structure, forced by the presence in the central core of the molecule of a spiro moiety, as shown in Figure 1a. As a consequence, such molecular HTM has excellent pore-filling ability,[2,3] coupled to the concomitant ability to provide hole extraction. However, after six years of persistent use as a sort of benchmark in PSC development, attempts to substitute it with other HTMs are ongoing,[4–7] due to several factors that strongly limit the commercialization of PSCs containing it. In particular, the costs of production and the lack of chemical stability that ultimately affects PSC performances after prolonged time.[8] Furthermore, SPIRO requires an oxidation step for implementation as a HTM[9]: up-to-date, the benchmark process[10] involves the use of two additives, namely tert-butylpyridine (tBP) and lithium bis(trifluoromethylsulfonyl)-imide (LiTFSI) (see Figure 1) in a nitrogen-saturated atmosphere, followed by overnight storage in a drybox to allow the complete oxidation of the HTM. In order to explain the high hole mobility achieved after proper doping [11,12] Abate et al. in a seminal work [13] proposed a two-step mechanism for the formation of Spiro-OMeTAD$^{\cdot+}$ (from now SPIRO^{+}) from the neutral molecule, in the presence of oxygen and LiTFSI:

$$SPIRO + O_2 \overset{h\nu}{\rightleftarrows} SPIRO^{\cdot+}O_2^{\cdot-} \quad (1)$$

$$SPIRO^{\cdot+}O_2^{\cdot-} + LiTFSI \overset{h\nu}{\leftrightarrows} SPIRO^{\cdot+}TFSI^{-} + Li_xO_y \quad (2)$$

in which Li_xO_y represents mixed Li_2O and Li_2O_2 oxides, produced by $TFSI^-$ anion exchange and reduction of superoxide anion O_2^-. The same mechanism was proposed in other studies focusing on SPIRO$^{\cdot+}$ radical formation[11] and investigating the effect of tBP on the HTM morphology[1,14] and

solar cell efficiencies.[15] However, none of the mentioned works paid attention on whether tBP also affects the HTM conductivity (except for a single work highlighting the negative effect of tBP on charge injection efficiency in dye-sensitized solar cells).[16] Indeed, the proposed mechanism only considers the involvement of oxygen and LiTFSI, without emphasizing the presence of tBP, that in standard recipes[17] is actually used in large excess with respect to the other constituents (about 3 times more than SPIRO and 6 times more than LiTFSI). More recently, some interesting works dealing with the interaction between SPIRO and tBP appeared, investigating the formation of a pyridinated derivative after light soaking the HTM and the structural modifications (i.e. crystallization *vs* amorphous state) that can take place when tBP is used in the HTM [18,19].

Although all these works are very convincing and strengthen the active role of tBP in determining SPIRO behavior in PSCs, none of them discusses directly the structure-property relationships between the solid-state microstructure and the hole-extraction ability of these molecular HTM, that is the most important information to consider for photovoltaic applications.

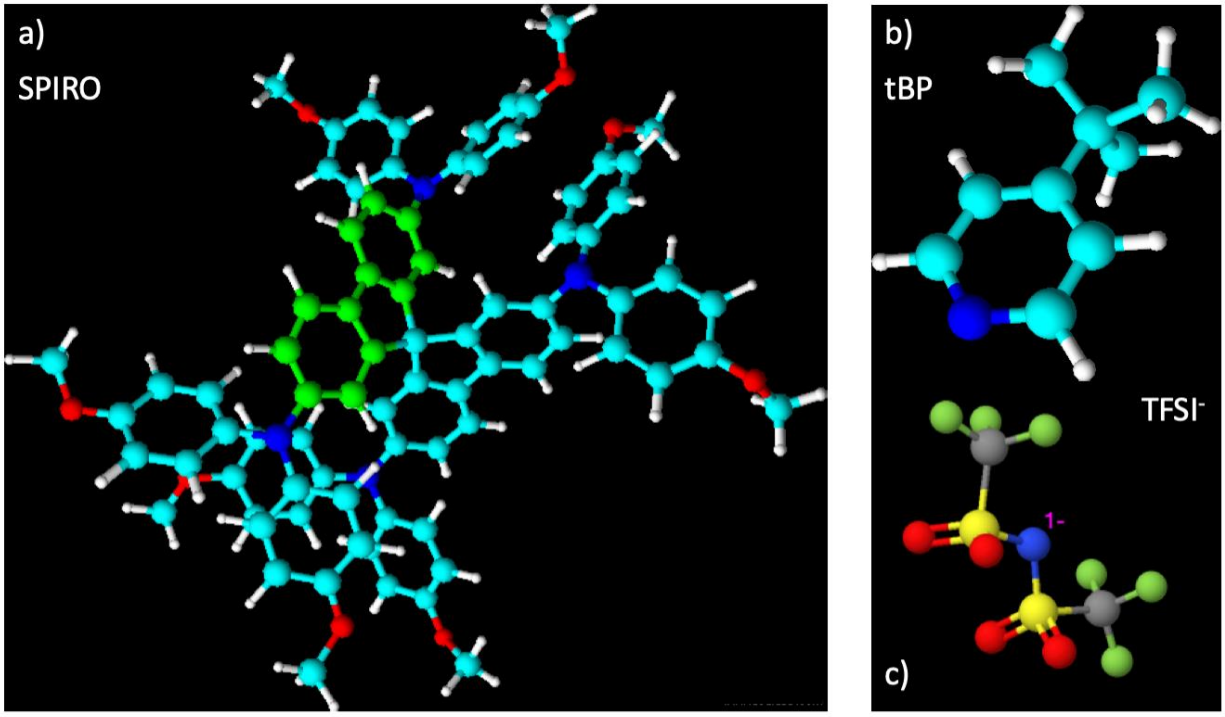

Figure 1. The chemicals used for the preparation of SPIRO-based HTMs depicted in 3D view. a) Spiro-OMeTAD (SPIRO) – some carbon atoms are green-painted to highlight the lack of co-planarity due to the presence of the central spiro moiety; b) tert-butyl pyridine (tBP); c) lithium bis(trifluoromethylsulfonyl)-imide (LiTFSI) (here Li^+ ion is not displayed).

For this reason, in this work we carry out an insightful spectroscopic study on SPIRO-based HTMs used in PSCs, experimentally highlighting the detrimental effect of tBP addition that causes a de-doping of the HTM, through a mechanism consistently linked to the structural changes taking place in the SPIRO molecule after oxidation. It is important to underline how the knowledge of the structural phase of SPIRO molecules in the HTM state can become fundamental for determining the contribution to the overall cell conductivity due to the HTM itself. In a recent work by Bakr and co-workers, the authors experimentally determined the hole mobility of a SPIRO single-crystal and found it comparable to that obtained with the oxidized SPIRO molecule in the solid state when used as a thin film within a PSC.[12]

The presence of an unpaired electron in $SPIRO^+$ prompted us to employ Electron Spin Resonance (ESR) spectroscopy as a powerful tool for the characterization of this molecular radical

with high selectivity and sensitivity, as recently reported.[11,13] Raman spectroscopy is then applied for investigating the structural modifications occurring in time in the prepared HTMs.

Results and Discussion

The analytical procedure requested the preparation of different tubes for ESR containing each one of four samples. The first sample contains an organic solution of all the three components within the SPIRO-based HTM material, i.e., SPIRO, LiTFSI and tBP, according to the standard literature procedure.[20] The solvent – a mixture of acetonitrile and dichlorobenzene, as reported in the Experimental Procedure - is then quickly removed under vacuum and a film is formed on the tube surface (SPIRO:LiTFSI:tBP sample). A second tube was prepared similarly but without tBP (SPIRO:LiTFSI sample). The third one, then, without LiTFSI (SPIRO:tBP sample) and the forth one with only the pure organic compound (SPIRO sample). The experimental procedure is sketched in Figure 2 for the sake of clarity.

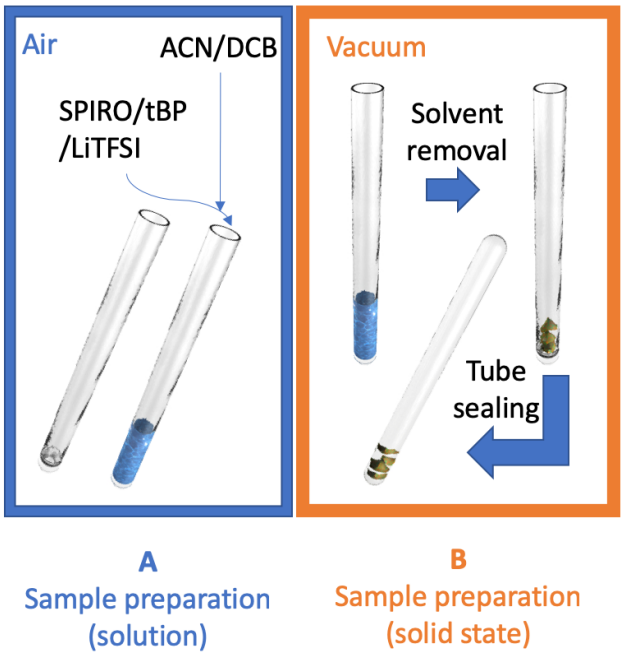

Figure 1. Pictorial sketch depicting the experimental procedure used for the preparation of the two kinds of samples (namely, the ones in solution (A) and the ones in solid state (B)) used for ESR characterization.

In dark, SPIRO:LiTFSI provides an intense ESR line originated from a radical species (Figure 3a, green curve. A lamp on/off is added to ESR figures from now on to indicate that data are collected, respectively, in light/dark conditions). The line position (also called g-factor, i.e. the ratio between the spectrometer working frequency and the magnetic field) in the spectrum, although not fully corresponding to the literature value[11] (g = 2.0045 vs g = 2.0030) is clearly associated with the ESR spectrum of the $SPIRO^{+\cdot}$ radical cation. The slight differences in g-factor values could derive from the different experimental conditions used for the preparation of the films.

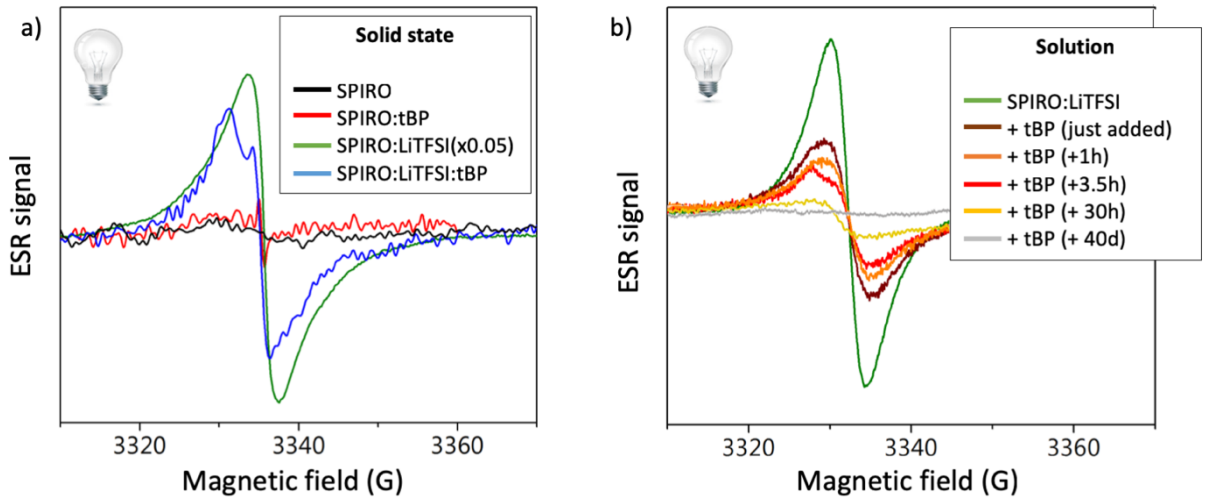

Figure 3. ESR analysis on the SPIRO molecule after tBP addition in solid state (a) and acetonitrile dichlorobenzene mixed solution (b). SPIRO:LiTFSI signal was reduced by a factor of 20 to improve data visualization.

Addition of tBP affects significantly the ESR peak intensity and shape (Figure 3a, blue line), as well as any ESR signal can be found for the control samples (namely, SPIRO and SPIRO:tBP samples) (Figure 3a, red and black lines). In addition, a decrease in time of the $SPIRO^{+\cdot}$ radical signal in dark is observed for the SPIRO:LiTFSI:tBP sample, as shown in Figure S1, suggesting a time-dependent effect due to interactions among the additives or morphological rearrangements in the solid state. In order to confirm this hypothesis, the same study is performed in liquid (Figure

3b) where the quenching effect of tBP on a similar ESR signal is found with a faster kinetics than in the solid state, due to enhanced diffusion. On the other hand, it is peculiar the absence of any change in the line-shape of the signal in liquid compared to the solid state: the line-shape of the signal from the SPIRO:LiTFSI:tBP solid sample (blue line, Fig. 3a) probably reflects the similar line-shape found in solution (in the +3.5 h sample in Fig. 3b, red curve). However, this signal disappears in time and it probably indicates the occurrence of a radical-based process within the sample.

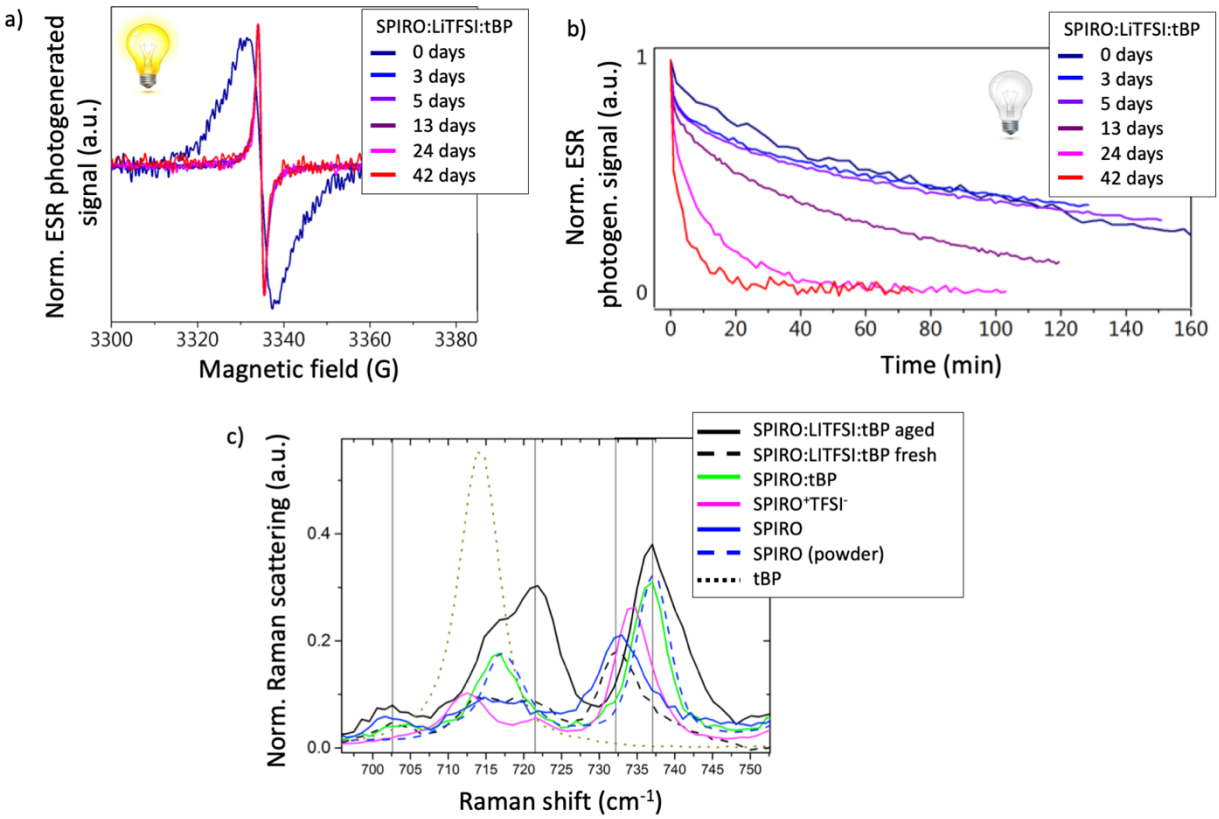

Figure 4. Physico-chemical evidences of the phase transition occurring in the SPIRO solid sample. (a) Light induced (light on - light OFF) ESR spectra of SPIRO:LiTFSI:tBP in the solid state and (b) Time traces of ESR intensity after light OFF in SPIRO:LiTFSI:tBP, at different days after sample preparation; some lines in panel (a) are very similar, therefore impossible to distinguish one from the other. (c) Raman analysis of the different SPIRO-based HTMs in the solid state. In particular, "SPIRO (powder)" refers to the reagent-grade SPIRO material taken as a solid, while the reference sample "SPIRO$^+$TFSI$^-$" is obtained by removing the solvent in vacuo from the solution of SPIRO:LiTFSI.

Since tBP in the solid state alters not only the intensity of the ESR peak (i.e. the number of spins) but also the line-shape (i.e. the structural phase in which the SPIRO molecule is arranged), a deeper investigation on the interactions occurring between light and the materials is carried out, in order to gain further insights into the causes of the observed quenching effect.

When the light is switched on, a broad peak (Figure 4a, dark blue line) is generated and the difference between the light-on and light-off ESR spectra is reported in Figure 4a. In addition, by following the evolution of the ESR signal over several days, a marked change in the shape of the ESR line takes place, associated to a narrowing of the peak.

The kinetics of light-induced generated radicals and their subsequent decays are examined by considering the time evolution of the ESR spectra after switching on the light and after switching off the light, in a time scale of several minutes. Moreover, the formation and decay traces are recorded on the same sample several days after its preparation. The kinetic traces, reported in Figure 4b, show a continuous change in the ESR signal decay within a period of several days, suggesting an evolution of the solid mixtures which accelerates the light-induced formation and consequent decay of the $SPIRO^{\cdot+}$ radical. Altogether, these results confirm that the oxidations occurring in the solid state – i.e. the ones that take place during the oxidation step of an HTM within a PSC stored in a drybox – is far from the simple mechanism considered valid up to now (eq. 1 and 2).

The small linewidth in aggregates is generally due to the fast exchange narrowing normally occurring in highly concentrated radical samples. The high concentration of radicals in the SPIRO:LiTFSI sample evidently produces the observed narrowing of the ESR line. Furthermore, the broader peak is related to several $SPIRO^{+}$ isolated species. For this reason, the narrow

contribution previously found in the ternary HTM SPIRO:LiTFSI:tBP (Figure 3, blue line) ESR spectrum can be now easily attributed to aggregated $SPIRO^+$ domains.

A fast decay is usually related to the presence of a crystalline profile in a semiconductor (i.e. a lower number of traps within the optical band-gap), suggesting that an amorphous to crystalline transition phase takes place in tBP-rich environments. This hypothesis is supported by Raman analysis of the different sample (Figure 4c). At first sight indeed, a slight shift towards higher energies of the peak at 732.5 cm^{-1} is found for every samples in which SPIRO aggregates were detected through ESR. The reagent-grade SPIRO powder – taken as the reference for a crystalline phase – has the highest shift together with the samples containing tBP. This peak is attributed to a_1 fundamental mode of fluorenes[21] (the two twisted central parts of the SPIRO molecule sharing a carbon atom) and its shifting towards higher energies (i.e. an increasing of the phonon frequency) is due to a compression of the lattice parameters. This evidence further confirms that tBP favors a less amorphous state for SPIRO molecules.

In addition, the peak at 722 cm^{-1} is attributed to the $TFSI^-$ anion coordinated by $SPIRO^+$ species, since $TFSI^-$ Raman spectrum is known to be affected by ionic coordination [22–24] and being visible only in SPIRO-based samples containing LiTFSI. Moreover, the reference sample $SPIRO^+TFSI^-$ is obtained by simply removing the solvent from the pink solution of SPIRO:LiTFSI, thus allowing us to consider it as the oxidized form of SPIRO, stated as $SPIRO^+TFSI^-$. Nothing can be said of the peaks in the 710-720 cm^{-1} region, because of the strong signal of tBP that does not allow a fruitful interpretation of the peaks.

In order to deepen our knowledge of the SPIRO-based HTM and of the effects of additives on carriers life-time, ESR analysis was carried out under illumination since, in this condition, the ESR signals of all samples increases although with different intensities, kinetics and shapes (Figure S2).

In particular, in the SPIRO:LiTFSI:tBP the broader line increases under light irradiation so that the narrower cannot be detected, whereas in the other samples it is the narrow line which is increased by light. The kinetics of formation and decay of the ESR lines are reported in Figure S2. The signal in SPIRO:tBP increases with a relatively fast kinetics (a few minutes, Figure S2b), whereas the signal in SPIRO:LiTFSI increases with a much slower rate (several hours, Figure S2c).

The first conclusion to be derived from these data is that, in dark, tBP inhibits the formation of the $SPIRO^+$ species. On the other hand, when the film is continuously irradiated, the tBP-mediated $SPIRO^+$ quenching process is not the dominant process and the oxidation of SPIRO molecules takes place, although less efficiently than in the SPIRO:LiTFSI sample. However, a light soaking phenomenon (i.e. the formation of persistent $SPIRO^+$ species by means of light irradiation) is efficient only in absence of tBP. The second conclusion is that an oxygen-free oxidation of SPIRO is possible for both SPIRO species (i.e. isolated SPIRO molecules embedded in the film) and aggregated SPIRO.

It is evident that tBP has an active role in determining the electronic properties of SPIRO-based HTMs, but it is not clear whether it is possible to correlate these ESR data to the real processes happening within a PSC. It is reported that tBP increases the film wettability:[14,25] this evidence is in agreement with the chemical nature of tBP, that is a high boiling point liquid and, being impossible to totally remove it during HTM processing through spin-coating on top of the perovskite, it allows the formation of a viscous layer that helps the SPIRO molecules to diffuse. This diffusion then creates some “aggregates of SPIRO molecules”, that increase the number of active $SPIRO^+$ species. This evidence is corroborated by a study of Juarez-Perez et al.[1] in which they showed the formation of segregated domains in doped SPIRO samples (i.e. with the addition

of LiTFSI and tBP). Furthermore, we observed that in SPIRO:LiTFSI sample solution, flocculation of white particles occurs quickly, as also reported elsewhere.[14] The Raman measurement of the precipitate unequivocally denotes it as LiTFSI (Figure S3), by the presence of the main peak at 749 cm^{-1} (related to the symmetric deformation of the $-CF_3$ group in the $TFSI^-$ anion)[26]. We can state therefore that tBP helps the solubilization of the LiTFSI salt [27] in dichlorobenzene solution, allowing the availability of $TFSI^-$ anion for $SPIRO^+TFSI^-$ species formation.

The aggregated SPIRO signal in solid state maintains its characteristic behavior (i.e. ESR intensity and slow kinetics) during aging: after 18 days the amount of photogenerated $SPIRO^+$ species and the rate at which they are formed, are unaltered (Figure S4).

The ESR signal of SPIRO:tBP control sample shows a rearrangement of the materials (Figure S5). Following the kinetics of radical formation within the film SPIRO:tBP (Figure S5c-d) we detect a little variation of the ESR signal in dark (Figure S5a), whereas the kinetics remain unchanged after illumination (Figure S5b-c-d). This result confirms that in solid state the efficiency of photogeneration is kept constant for the aggregated SPIRO molecules.

At this point, the interpretation of the behavior of SPIRO:LiTFSI+tBP solid state sample is straightforward. In dark (Figure 3a-b), we observe that $SPIRO^+$ is decreased by tBP addition. After 40 days, no $SPIRO^+$ is visible any more. More interestingly, the photogenerated ESR spectra (Figure 4a) changes from solvated $SPIRO^+$ (broad ESR line) to aggregated $SPIRO^+$ species (narrow ESR line). The kinetics of quenching of photogenerated $SPIRO^+$ after switching off the light (Figure 4b) is very slow (due to the presence of tBP) in a freshly prepared sample, and much faster in an aged sample, similarly to a SPIRO:tBP blend without LiTFSI.

This scenario prompted us to give an overall interpretation of the occurring phenomena in SPIRO-based HTM. The tBP is able to react with the radical $SPIRO^{+}$.[19] However, being the tBP a high-boiling point liquid and therefore un-removable from the HTM, in solid state it also allows the rearrangement of SPIRO molecules by slowly increasing the crystallinity[12] of the domains of the HTM in its semi-liquid environment. Therefore, among the already recalled morphological/solubilizing effects of tBP in SPIRO-based HTMs, this species also has an active role in affecting the overall crystallinity of the film. However, this action is completed in relatively longer times compared to the other effects.

Soon after the SPIRO film formation in dark, LiTFSI promotes the generation of $SPIRO^{+}$ species by electron transfer to molecular oxygen followed by anion exchange and formation of $SPIRO^{+}TFSI^{-}$ domains. However, in the presence of tBP, the concentration of SPIRO cation is kept relatively low as demonstrated by ESR spectra. The effect of light irradiation (light soaking) is to increase dramatically the generation of $SPIRO^{+}$ species.

More in detail, the chemical role of tBP affects LiTFSI solubility in a chlorobenzene environment, by allowing the dissociation of LiTFSI and thus providing solvated $TFSI^{-}$ ions in solution that may react with $SPIRO^{+}$ producing solid domains of $SPIRO^{+}TFSI^{-}$ and lithium mixed oxides (eq. 3):

$$LiTFSI + SPIRO^{+}O_2^{-} + tBP \rightarrow Li_xO_y + SPIRO^{+}TFSI^{-} + tBP \qquad (3)$$

After a while, the morphological role of tBP, affecting SPIRO crystallinity, starts to be relevant in the process. By means of ESR we are able to distinguish between amorphous SPIRO and crystalline SPIRO, made by aggregated SPIRO molecules, (namely, $SPIRO^{\cdot+}_{(free)}$ and $SPIRO^{\cdot+}_{(agg)}$ species).

In the case of the SPIRO:LiTFSI sample, lacking tBP, the formation of aggregated $SPIRO^+$ species in a crystalline phase occurs instantaneously. However, the absence of tBP may alter the solubilization of LiTFSI affecting the availability of $TFSI^-$ anion for the formation of highly doped $SPIRO^+$ species.

This means that the morphological role of tBP is not only restricted to film wettability during HTM processing, but it also includes the stable creation of SPIRO aggregates that form an electron-acceptor density of states distribution close to the HOMO band, with a consequent increase of the hole-carriers equivalent mobility.[28] Indeed, the higher mobility in the organic semiconductor used as HTM is obtained by defect-induced doping. Generating electron-acceptor defects in the SPIRO band-gap close to the HOMO is equivalent to doping the SPIRO, consequently shifting the Fermi level toward the HOMO band. This situation is achieved only when this defect-induced density of states is very close to the HOMO level of SPIRO molecule, as demonstrated by Fantacci et al.[9]

Therefore, from one side the presence of tBP is required for increasing LiTFSI solubility in dichlorobenzene, so that instantaneously a density of states within the SPIRO bandgap is generated (i.e. a proper oxidation of SPIRO takes place), while from the other, tBP acts as a competitor in the time-dependent reaction of $SPIRO^+$ species formation, by inducing phase segregation inside the HTM (i.e. the formation of both amorphous and crystalline phases), which is an irreversible process.

In order to better understand whether tBP has a positive or negative impact on the HTM electronic properties, we performed 4-probe measurements on spin-coated thin films (Figure S6) showing that aggregated crystalline SPIRO layers (aged HTM with tBP) are less conductive than amorphous SPIRO layers (fresh HTM with tBP) and thus validating the ESR results, pointing out

at the existence of a lower amount of defects in the SPIRO band gap and the induction of an irreversible de-doping process. This macroscopic evidence suggests that a crystalline SPIRO-based HTM (an aged, de-doped one) can be detrimental for the solar cell, by negatively affecting the fill factor that is usually linked to the conductivity of the selective layers.

It is now required to unravel a chemical process though which SPIRO+ molecules undergo the de-doping detected through ESR.

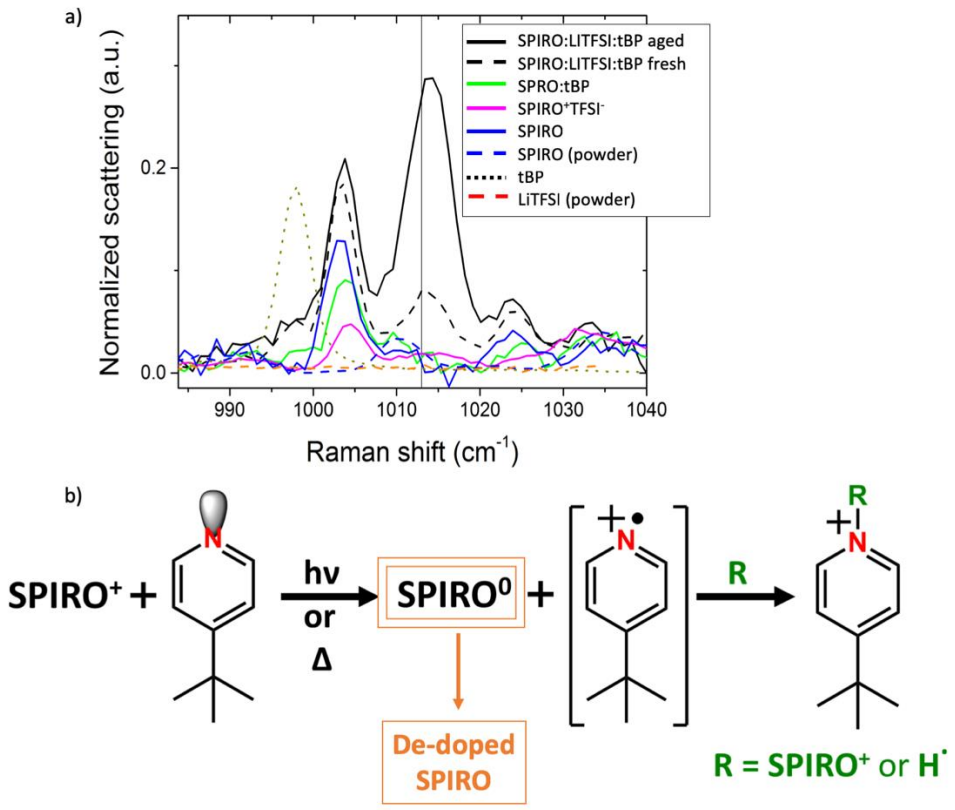

Figure 5. a) Effect of tBP addition on a SPIRO-based HTM. Raman spectra showing evidence of tert-butyl pyridinium formation at 1012 cm^{-1}. Caption details: "SPIRO (powder)" refers to the reagent-grade SPIRO material taken as a solid; the reference sample "$SPIRO^{+}TFSI^{-}$" is obtained by removing the solvent in vacuo from the solution of SPIRO:LiTFSI. b) Proposed mechanism for SPIRO de-doping in the presence of excess tBP.

In Figure 5, the Raman spectra of different samples around 1000 cm^{-1} are shown. A distinct peak centered at 1012 cm^{-1} is visible in samples containing both $TFSI^-$ and tBP. This Raman peak was already attributed to pyridinium cation species.[29,30] The formation of a *tert*-butyl pyridinium cation (tBP^+), as a part of a pyridinated covalent adduct between $SPIRO^+$ molecules and tBP, was recently reported by Kasparavicius et al.[19] Therefore a direct reaction of the tBP with the $SPIRO^+$ is responsible for a quenching of the radical in the material. In addition, one can expect that $TFSI^-$ acts as the counter-anion for tBP^+, as happens for well-known pyridinium-based ionic liquid.[31] The formation of such tBP^+ species proceeds though a chemical mechanism which is described in Figure 5b. In this process, a one-electron reduction of $SPIRO^+$ molecules takes place by means of tBP molecules (which are present in large excess within the HTM mixture). This generates a de-doped SPIRO (neutral species) and a *tert*-butyl pyridinium radical cation, which is an unstable intermediate (in square brackets in Figure 5b) and therefore, even if it is a radical, it is not detected through ESR. The pyridinium radical cation immediately reacts indeed with another $SPIRO^+$ molecule, leading to the pyridinated adduct between SPIRO and tBP previously reported in reference [19]. Such an adduct is a charged species, but do not contains un-paired electrons and it is also therefore invisible to ESR. In addition, since it contains a pyridinium cation within its molecular structure, it is responsible for the intense Raman signal that we detect at 1012 cm^{-1}. Finally, the positive charge on the cationic species is compensated by the presence of $TFSI^-$ anions. We also propose an alternative route for the formation of tBP^+ species (again in Figure 5b), which counts for the extraction of a hydrogen radical (H•) from a neutral tBP molecule by means of the tBP radical cation intermediate. The hydrogen radical is likely taken from the *tert*-butyl residues and the process can take place reasonably because of the large excess in tBP present in the HTM mixture. The product of this radical reaction if again a pyridinium cation, bearing $TFSI^-$ as counter-

anion, whose existence can again be related to the Raman signal at 1012 cm^{-1}. The fate of the radicals generated after hydrogen extraction can then be multiple and difficult to unravel. A possible route can involve the pairing of two radicals to form a dimer, but also other complex radical process can take place.

Conclusions

In conclusion, in this work we evidenced for the first time an active role of tert-butyl pyridine (tBP) in SPIRO-based hole transporting layers for PSC that impressively affects both the internal structural characteristic of this HTM and its electronic properties. In detail, the addition of tBP creates a semi-liquid environment in solid films that allows the structural reorganization of the SPIRO molecules, quickly rearranging from an amorphous state to a more crystalline structure. ESR and Raman analyses suggest that a de-doping mechanism occurs within the HTM inducing such an irreversible reorganization of the molecules. Being the first time this mechanism is proved to the best of our knowledge, it goes against the general conception of SPIRO as an amorphous HTM, able to passivate perovskite interfacial defects. It further suggests that the great advantage of the SPIRO HTM production process (i.e. the use of high-boiling point tBP) is limited to the morphological role of tBP, that permits solid state diffusion of molecules with consequent pinhole passivation. However, tBP induces also a fast de-doping of the doped SPIRO HTM, by the chemical interaction with $SPIRO^{+}$ providing tert-butyl pyridinium cations (as suggested by [19] and indicated here by our Raman data) $TFSI^{-}$ counter-anions, that have the major effect to reduce the overall conductivity of the SPIRO layer (proved by 4-probe measurements). This may consequently affect the fill-factor in a PSC.

Therefore, being SPIRO a defect-mediated HTM, the fact of using a trap quencher such as tBP becomes a limiting factor for its performance in PSCs.

Experimental Procedure

Samples preparation. Standardized recipe[17] is used for preparing SPIRO solutions containing 56 mM SPIRO (Lumtec), 32 mM LiTFSI (Sigma Aldrich) and 195 mM tert-Butylpyridine (tBP, Sigma Aldrich) in a dichlorobenzene:acetonitrile mixed solvent. All solvents are purchased from Sigma Aldrich. Several solutions were prepared: a) Fresh SPIRO only (labelled SPIRO sample); b) Fresh SPIRO with LiTFSI and tBP (labelled SPIRO:LiTFSI:tBP sample); c) Fresh SPIRO without LiTFSI with tBP (labelled SPIRO:tBP); d) Fresh SPIRO with LiTFSI without tBP (labelled SPIRO:LiTFSI sample); e) tBP only (labelled tBP sample). The solutions were prepared in glovebox under nitrogen atmosphere until used.

ESR measurements. All ESR measurements were performed on a Bruker ELEXSYS E580 spectrometer at X-band (9-10 GHz) mounting an ER4118X-MD5 dielectric cavity. Measurements were carried at 80 K, employing a liquid-N_2 cooling system. Continuous-wave spectra were typically acquired at 20-40 μW microwave power and 0.8 G field modulation amplitude. ESR measurements were conducted A) in solution/air (some drops of the solution is put into an ESR quartz tube open in air) or B) in film/vacuum (the solvent is evaporated out of the sample tube and the resulting solid film is left at the bottom and on the tube inner surface; the tube is then sealed under vacuum at ~10^{-5} bar). ESR spectra were recorded in dark conditions or in light by exposing the sample to white light.

Raman measurements. Using a inVia Renishaw instrumentation, spectra were recorded exploiting as excitation source a laser diode at 785 nm at a power of 1 W/cm2. The system has been calibrated against the 520.5 cm^{-1} line of an internal silicon wafer. The spectra have been registered in the 200–3000 cm^{-1} range. The final data have been averaged over 100 accumulations

in order to maximize the signal to noise ratio. The measurements were conducted at room temperature on solid blend deposited into ESR tubes, using the 5x objective.

Supplemental Information.

Additional experimental work is included in the Supplemental Information available free of charge.

Acknowledgements

This work is financially supported by OPERA project of "Centro Studi di Economia e Tecnica dell' Energia Giorgio Levi Cases" of the University of Padova.

Author contribution

Conceptualization, F.L., E.C., T.G., L.F.; Methodology, F.L., E.C., T.G., A.R.; Validation, F.L., E.C., R.S.; Investigation, F.L., E.C., T.G., R.S.; Resources, M.M., A.P., G.M.; Writing – Original draft F.L., T.G., L.F.; Writing – Review & editing F.L., T.G., A.R., E.M., M.M., A.P., L.F.; Supervision F.L., L.F.; Project administration E.M, G.M., M.M., L.F.; Funding acquisition E.M, G.M., M.M., L.F.

Declaration of interest

The authors declare no competing interests.

REFERENCES.

1. Juarez-Perez, E.J., Leyden, M.R., Wang, S., Ono, L.K., Hawash, Z., and Qi, Y. (2016). Role

of the Dopants on the Morphological and Transport Properties of Spiro-MeOTAD Hole Transport Layer. Chem. Mater. *28*, 5702–5709.

2. Ding, I.-K., Tétreault, N., Brillet, J., Hardin, B.E., Smith, E.H., Rosenthal, S.J., Sauvage, F., Grätzel, M., and McGehee, M.D. (2009). Pore-Filling of Spiro-OMeTAD in Solid-State Dye Sensitized Solar Cells: Quantification, Mechanism, and Consequences for Device Performance. Adv. Funct. Mater. *19*, 2431–2436.

3. Docampo, P., Hey, A., Guldin, S., Gunning, R., Steiner, U., and Snaith, H.J. (2012). Pore filling of spiro-OMeTAD in solid-state dye-sensitized solar cells determined via optical reflectometry. Adv. Funct. Mater. *22*, 5010–5019.

4. Kim, H.-S., Lee, C.-R., Im, J.-H., Lee, K.-B., Moehl, T., Marchioro, A., Moon, S.-J., Humphry-Baker, R., Yum, J.-H., Moser, J.E., *et al.* (2012). Lead Iodide Perovskite Sensitized All-Solid-State Submicron Thin Film Mesoscopic Solar Cell with Efficiency Exceeding 9%. Sci. Rep. *2*, 591.

5. Zhou, W., Wen, Z., and Gao, P. (2018). Less is More: Dopant-Free Hole Transporting Materials for High-Efficiency Perovskite Solar Cells. Adv. Energy Mater. *8*, 1702512.

6. Gatti, T., Casaluci, S., Prato, M., Salerno, M., Di Stasio, F., Ansaldo, A., Menna, E., Di Carlo, A., and Bonaccorso, F. (2016). Boosting Perovskite Solar Cells Performance and Stability through Doping a Poly-3(hexylthiophene) Hole Transporting Material with Organic Functionalized Carbon Nanostructures. Adv. Funct. Mater. *26*, 7443–7453. Available at: https://onlinelibrary.wiley.com/doi/abs/10.1002/adfm.201602803.

7. Gatti, T., Lamberti, F., Topolovsek, P., Abdu-Aguye, M., Sorrentino, R., Perino, L., Salerno, M., Girardi, L., Marega, C., Rizzi, G.A., *et al.* (2018). Interfacial Morphology

Addresses Performance of Perovskite Solar Cells Based on Composite Hole Transporting Materials of Functionalized Reduced Graphene Oxide and P3HT. Sol. RRL *2*, 1800013. Available at: https://onlinelibrary.wiley.com/doi/abs/10.1002/solr.201800013.

8. Arora, N., Dar, M.I., Hinderhofer, A., Pellet, N., Schreiber, F., Zakeeruddin, S.M., and Grätzel, M. (2017). Perovskite solar cells with CuSCN hole extraction layers yield stabilized efficiencies greater than 20%. Science (80-.). *358*, 768–771. Available at: http://science.sciencemag.org/content/sci/358/6364/768.full.pdf.

9. Fantacci, S., De Angelis, F., Nazeeruddin, M.K., and Grätzel, M. (2011). Electronic and Optical Properties of the Spiro-MeOTAD Hole Conductor in Its Neutral and Oxidized Forms: A DFT/TDDFT Investigation. J. Phys. Chem. C *115*, 23126–23133.

10. Burschka, J., Pellet, N., Moon, S.-J., Humphry-Baker, R., Gao, P., Nazeeruddin, M.K., and Grätzel, M. (2013). Sequential deposition as a route to high-performance perovskite-sensitized solar cells. Nature *499*, 316–319.

11. Namatame, M., Yabusaki, M., Watanabe, T., Ogomi, Y., Hayase, S., and Marumoto, K. (2017). Direct observation of dramatically enhanced hole formation in a perovskite-solar-cell material spiro-OMeTAD by Li-TFSI doping. Appl. Phys. Lett. *110*, 123904.

12. Dong, H., Shi, D., Hu, W., He, Y., Li, T., Zhong, C., Xu, W., Bakr, O.M., Pan, J., Li, Y., *et al.* (2016). Spiro-OMeTAD single crystals: Remarkably enhanced charge-carrier transport via mesoscale ordering. Sci. Adv. *2*, e1501491.

13. Abate, A., Hollman, D.J., Teuscher, J., Pathak, S., Avolio, R., D'Errico, G., Vitiello, G., Fantacci, S., and Snaith, H.J. (2013). Protic Ionic Liquids as p-Dopant for Organic Hole Transporting Materials and Their Application in High Efficiency Hybrid Solar Cells. J. Am.

Chem. Soc. *135*, 13538–13548.

14. Wang, S., Sina, M., Parikh, P., Uekert, T., Shahbazian, B., Devaraj, A., and Meng, Y.S. (2016). Role of 4- tert -Butylpyridine as a Hole Transport Layer Morphological Controller in Perovskite Solar Cells. Nano Lett. *16*, 5594–5600.

15. Wang, S., Huang, Z., Wang, X., Li, Y., Günther, M., Valenzuela, S., Parikh, P., Cabreros, A., Xiong, W., and Meng, Y.S. (2018). Unveiling the Role of tBP–LiTFSI Complexes in Perovskite Solar Cells. J. Am. Chem. Soc. *140*, 16720–16730. Available at: https://doi.org/10.1021/jacs.8b09809.

16. Katoh, R., Kasuya, M., Furube, A., Fuke, N., Koide, N., and Han, L. (2009). Quantitative study of solvent effects on electron injection efficiency for black-dye-sensitized nanocrystalline TiO2 films. Sol. Energy Mater. Sol. Cells *93*, 698–703.

17. Tao, C., Van Der Velden, J., Cabau, L., Montcada, N.F., Neutzner, S., Srimath Kandada, A.R., Marras, S., Brambilla, L., Tommasini, M., Xu, W., *et al.* (2017). Fully Solution-Processed n-i-p-Like Perovskite Solar Cells with Planar Junction: How the Charge Extracting Layer Determines the Open-Circuit Voltage. Adv. Mater. *29*, 1604493.

18. Magomedov, A., Kasparavičius, E., Rakstys, K., Paek, S., Gasilova, N., Genevičius, K., Juška, G., Malinauskas, T., Nazeeruddin, M.K., and Getautis, V. (2018). Pyridination of hole transporting material in perovskite solar cells questions the long-term stability. J. Mater. Chem. C *6*, 8874–8878.

19. Kasparavicius, E., Magomedov, A., Malinauskas, T., and Getautis, V. (2018). Long-Term Stability of the Oxidized Hole-Transporting Materials used in Perovskite Solar Cells. Chem. - A Eur. J. *24*, 9910–9918.

20. Tao, C., Neutzner, S., Colella, L., Marras, S., Srimath Kandada, A.R., Gandini, M., Bastiani, M. De, Pace, G., Manna, L., Caironi, M., *et al.* (2015). 17.6% stabilized efficiency in low-temperature processed planar perovskite solar cells. Energy Environ. Sci. *8*, 2365–2370.

21. Lee, S.Y., and Boo, B.H. (1996). Density Functional Theory Study of Vibrational Spectra of Fluorene. J. Phys. Chem. *100*, 8782–8785.

22. Herstedt, M., Henderson, W.A., Smirnov, M., Ducasse, L., Servant, L., Talaga, D., and Lassègues, J.C. (2006). Conformational isomerism and phase transitions in tetraethylammonium bis(trifluoromethanesulfonyl)imide Et4NTFSI. J. Mol. Struct. *783*, 145–156.

23. Marczewski, M.J., Stanje, B., Hanzu, I., Wilkening, M., and Johansson, P. (2014). "Ionic liquids-in-salt" – a promising electrolyte concept for high-temperature lithium batteries? Phys. Chem. Chem. Phys. *16*, 12341–12349.

24. Brouillette, D., Irish, D.E., Taylor, N.J., Perron, G., Odziemkowski, M., and Desnoyers, J.E. (2002). Stable solvates in solution of lithium bis(trifluoromethylsulfone)imide in glymes and other aprotic solvents: Phase diagrams, crystallography and Raman spectroscopy. Phys. Chem. Chem. Phys. *4*, 6063–6071.

25. Hawash, Z., Ono, L.K., and Qi, Y. (2018). Recent Advances in Spiro-MeOTAD Hole Transport Material and Its Applications in Organic-Inorganic Halide Perovskite Solar Cells. Adv. Mater. Interfaces *5*, 1700623.

26. Hardwick, L.J., Holzapfel, M., Wokaun, A., and Novák, P. (2007). Raman study of lithium coordination in EMI-TFSI additive systems as lithium-ion battery ionic liquid electrolytes. J. Raman Spectrosc. *38*, 110–112.

27. Blackmore, I.J., Gibson, V.C., Hitchcock, P.B., Rees, C.W., Williams, D.J., and White, A.J.P. (2005). Pyridine N-Alkylation by Lithium, Magnesium, and Zinc Alkyl Reagents: Synthetic, Structural, and Mechanistic Studies on the Bis(imino)pyridine System. J. Am. Chem. Soc. *127*, 6012–6020.

28. Petty, M.C. (2007). Organic and Molecular Electronics: From Principles to Practice 1st ed. (John Wiley & Sons, Ltd).

29. Rogers, D.J., Luck, S.D., Irish, D.E., Guzonas, D.A., and Atkinson, G.F. (1984). Surface enhanced raman spectroscopy of pyridine, pyridinium ions and chloride ions adsorbed on the silver electrode. J. Electroanal. Chem. Interfacial Electrochem. *167*, 237–249.

30. Regis, A., and Corset, J. (1980). A chemical interpretation of the intense raman spectra observed at a silver electrode in the presence of chloride ion and pyridine: formation of radicals. Chem. Phys. Lett. *70*, 305–310.

31. Chaban, V. V., and Prezhdo, O. V. (2016). Ionic Vapor Composition in Pyridinium-Based Ionic Liquids. J. Phys. Chem. B *120*, 4661–4667.